Sorption-Deformation Interplay in Hierarchical Porous Polymeric Structures Composed of a Slit Pore in an Amorphous Matrix

Lingji Hua, Chi Zhang, Ali Shomali, Benoit Coasne, Dominique Derome, Jan Carmeliet

Sorption-deformation interplay in hierarchical porous polymeric structure composed of slit-pore in amorphous matrix

Lingji Hua[1], Chi Zhang[1], Ali Shomali[1], Benoit Coasne[2], Dominique Derome[3], and Jan Carmeliet[1]

[1] Chair of Building Physics, Department of Mechanical and Process Engineering, ETH Zürich (Swiss Federal Institute of Technology in Zürich), Zürich 8093, Switzerland

[2] Univ. Grenoble Alpes, CNRS, LIPhy, F-38000 Grenoble, France

[3] Department of Civil and Building Engineering, Université de Sherbrooke, Sherbrooke, QC, Canada

Wood, as a natural adsorbent and significant building material, features complex biopolymer composition and hierarchical porous structure, endowing it with distinguished sorption properties accompanied by sorption-induced deformation. In former molecular simulation studies, sorption, deformation and coupled sorption-deformation have been studied for single-scale materials, but scarcely for materials where micropores (< 2 nm) and mesopores (2-50 nm) coexist. The present work, dealing with a mesoscopic slit-pore between two slabs of amorphous and microporous cellulose, aims at modeling sorption and sorption-induced deformation in hierarchical cellulosic porous structures. Specifically, the atomic system is numerically modeled by a hybrid workflow combining molecular dynamics (MD) and grand canonical Monte Carlo (GCMC) simulations. The results clarify the multiple sorption/deformation mechanisms in the porous materials with different slit-pore sizes, including water filling in micropores, surface covering at slit-air interface and subsequent capillary condensation in mesopores. In particular, before capillary condensation, the sorption behavior of AC matrix of the hybrid system is almost the same as for bulk AC, in which sorption and deformation enhance each other through sorption-induced swelling and additional sorption in the newly-created voids. Upon capillary condensation, however, interaction between the micropores and mesopore emerges. Water molecules in mesopore exert a negative hydrostatic pressure or tensile stress perpendicular to the slab surface on the matrices, resulting in an increase in porosity and water content, a decrease in distance between the center of mass (COM) of the slabs and thus a thinning of the slit-pore. Notably, the micropore space in slabs induced by either sorption stress in matrices or capillary forces in slit-pores is saturated with water once it has been created. As described by Bangham's Law, the surface area of the rough slit-pore slab increases proportionally to surface energy variation during surface covering. For the system comprised by compliant polymers like AC, however, the surface area enlargement is not resulting in an in-plane swelling as expected, but in an in-plane shrinkage along with an increase in local roughness or irregularity (an accordion effect).

1. Introduction

Wood is a natural fuel and construction material that has been ubiquitously used for thousands of years[1]. In the past decades, through material modification and bio-mimetic technology, the application of wood, or wood-derived materials has further extended to emerging high-tech fields[1,2] like flexible electronics[2,3], clean energy[2–4], bioengineering[2,5], agriculture[5,6] and so on. Such advances are largely attributed to the growing knowledge on the morphology, structure and chemical composition of natural wood, which endow the material with its specific mechanical, thermal or optical properties[1,2]. Generally, wood is a lignocellulosic compound possessing multi-scale hierarchy in porosity, composed of the micrometer-or-millimeter-sized lumina surrounded by the cell walls, the micrometer-sized pits traversing the cell walls and the nano-sized pores distributed within the cell walls[1,7]. Notably, the nano-sized pores buried in the cell walls also exhibit hierarchy ranging from micropores (< 2 nm) to mesopores (~2 nm)[8,9]. Despite the similarity in the cell-wall composition (mainly cellulose, hemicellulose and lignin) and the general geometry, the variability in the cell-wall microstructure, cell size, shape and wall-to-lumen ratio leads to a large diversity in wood anatomy among tissue types and tree species[1].

Wood-moisture interaction induced by the hydrophilic composition or hierarchical porous structure is another intriguing topic, since wood-based materials in most practical scenarios are frequently subjected to changing moist atmospheres. Typical scenarios include but are not limited to the furniture or buildings exposed outside, the smart windows for optical regulation[3] and the water-retaining agents for plants[5,6]. To elucidate the mechanisms and effects of wood-moisture interaction, numerous experimental studies on the water sorption isotherms or dynamics in natural/engineered wood are reported[10–13]. Despite the variation in wood species, sample sizes and measurement methods, the produced adsorption isotherms display similar patterns like initial quick adsorption, steady increase midway and steep growth at near-saturation point[10]. Remarkable hysteresis throughout the hygroscopic range is commonly recognized, falling into none of the empirical classifications of International Union of Pure and Applied Chemistry (IUPAC)[14] and with hybrid feature[11]. There is also a consensus that the distinguished properties in wood-moisture sorption and hysteresis are a combined contribution of the coexisting micropores and mesopores in wood[11].

Meanwhile, the adsorbents composed of flexible bio-polymer like wood are subjected to substantial deformation. Such deformation is induced by the change of energy landscape in wood due to water presence, and will further impose counteractive effects on its sorption properties through the variation in pore size. With the development of microscopic imaging technologies, the anisotropic sorption-induced deformation in woods can be visualized and correlated to its inter-cell and intra-cell geometric anisotropy[15,16]. Meanwhile, non-homomorphic deformation is reported[17], suggesting an asynchronous swelling/shrinking in pores with different scales. It is also worth noting that hysteresis in sorption and swelling/shrinkage strain persist throughout the hygroscopic range[17,18]. Contact angle variation between capillary condensation and evaporation is a prevailing interpretation for sorption/strain hysteresis[10], but it can only account for the hysteresis under high RH in mesoscopic capillaries[14]. Instead, the coupling between sorption and deformation[19] can explain the all-region hysteresis in wood-moisture interaction. Such complicated pattern of deformation and its coupling to sorption further complexify the research in wood sorption-deformation coupling mechanism upon water sorption.

Despite the lack of quantitative analysis, it is widely accepted that the specific adsorption isotherm shape, the non-homomorphic deformation and the remarkable hysteresis in wood are largely

attributed to the compliant, hydrophilic matrix and the hierarchical porous structure ranging from micropores to mesopores. Advances in the mechanism of wood-moisture interaction are anticipated once the contribution of pores with different sizes is clarified and differentiated. However, since practical materials always display multi-scale hierarchy, long-range (compared to cell dimension) heterogeneity[16], complicated intrapore connectivity[17], irregular cracks and defects[17], this object is hardly achievable based on experimental observation only.

Molecular simulation is then proposed as a potential alternative to experiments, due to its flexibility in micro-structure construction and capability to convey atom-level information. Pre-existing wood-related studies based on molecular simulation are mainly focused on the cell-wall matrices without mesopores[20–22] and the relevant structure-property relationships[21–24]. Besides, except the work of Vandamme, previous sorption-related studies based on molecular simulation employ either purely microporous materials[25–27] or a standalone mesopore[28–30]. This author[31] has investigated the adsorption of carbon dioxide into a linear poroelastic coal bed methane reservoir with both micropores and mesopores. Regardless of the hierarchical nature in porous structure, this study assumes a universal sorption mechanism—surface covering for all pores. Accordingly, the sorption stress in the coal bed can be predicted by Gibbs' adsorption isotherm as

$$\Delta\gamma = -\int_{-\infty}^{\mu} \Gamma\left(\mu^*\right) d\mu^* \tag{1}$$

where γ, μ and Γ respectively denote the surface energy, chemical potential and surface adsorption amount per unit area. In brief, Eq.(1) states that the surface energy variation due to surface covering is an integral of adsorbed density with respect to chemical potential.

Wood is different from the coal bed since it is made up of an amorphous cluster of polymer chains adsorbing water molecules not only via surface covering but also by water filling in the micropores and capillary condensation in the mesopores. Molecular simulation on such nonlinear flexible polymers with multiple sorption mechanisms is not available, leaving a niche in the computational investigation of the sorption-deformation coupling in hierarchical porous structure.

Here, in this study, we attempt to elucidate the mechanism of sorption-deformation coupling in wood cell wall by means of molecular simulation on a wood-inspired model structure: a hierarchical porous structure encompassed by soft, hydrophilic bio-polymers. The first part of this paper is dedicated to the methodology in model structure construction, simulation implementation, data reduction and treatment. The obtained results are then analyzed in the second part, followed by a discussion on the implication of our study, along with its limitation and improvement direction. This work is then summarized in a conclusion.

2. Methodology

2.1 Objective of Research

This work aims to grasp the sorption-deformation characteristics in wood, as driven by the soft, hydrophilic matrices with hierarchical porosity, based on molecular simulation. However, given the limitation in speed and size of current molecular computing technology, it is almost infeasible to replicate all chemical and structural details of natural wood in simulation. Hereby, the following simplifications are adopted to establish a system showing essential structural features and allowing computational feasibility.

1. Mainly focused on the structural effects, the chemical composition is simplified to pure amorphous cellulose, which is hydrophilic and flexible as wood cell walls.

2. Only one-layer of hierarchy is employed in porosity, namely, micropores naturally present among bio-polymers and a meso-scale pore (1-4nm) corresponding to the void formed between the microporous matrices.
3. Topological details of the pores are neglected and a simple structure of slit-pore is considered (Fig.1(a)).
4. To further lighten the computational burden, a slit-pore with two slabs of thin cell walls is isolated from Fig.1(a) and the constraint imposed by the omitted surrounding bulk material is supplemented by a linear spring connected between the centers of mass (COM) of the two slabs (Fig.1(b)). Spring forces will be generated once the COMs' distance deviates from the initial length and distributed to each cellulose atom with mass-weighted proportion.

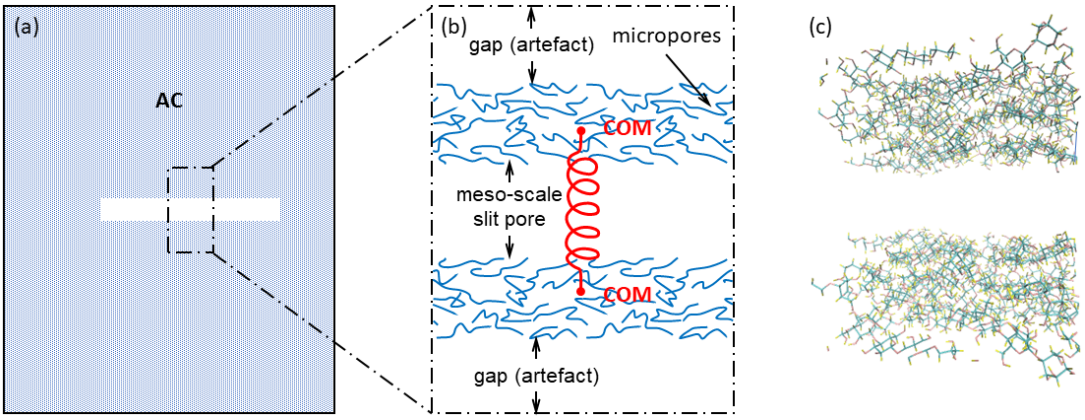

Fig 1 Schematic of the objective system. (a) A mesoscopic slit-pore (1-4 nm) buried in infinite microporous matrices consisting of amorphous cellulose. (b) A mesoscopic slit-pore (1-4 nm) sandwiched between two thin microporous slabs consisting of amorphous cellulose, with a spring mimicking the constraint imposed by the omitted surrounding framework in Fig.1(a). (c) 3D snapshot of the system constructed by molecular simulation software (as explained in the text).

As shown in Fig.1(c), the considered pore structure is a mesoscopic slit-pore (1-4 nm) sandwiched between two microporous slabs consisting of amorphous cellulose. This system captures the basic features of the hierarchical pores of interest (namely a mesopore embraced by microporous matrices) without introducing unnecessary geometric details. With the simplified chemical and structural components, this work is not aiming to reproduce the sorption and swelling isotherms in practical materials, but to shed light on the coupling mechanisms of sorption and deformation in naturally common materials possessing hierarchical porous structures.

2.2 Construction Method

The slit-pore system is constructed based on the workflow as shown in Fig.2. First of all, one chain of Iβ crystallite cellulose with 8 repeating β(1→4)-linked D-glucose units is created in the toolkit Cellulose-Builder[32]. Optimized potentials for liquid simulations (OPLS) forcefield in its all-atom (AA) version[32,33] with 1.14*CM1A-LBCC partial atomic charges[33] is employed to take account of the intra-molecular and inter-molecular forces in cellulose. The parameters are generated through a web-based service – LigParGen[34] and enumerated in **Supplementary Information Note I**. The Lennard-Jones (LJ) potential is cut off beyond the distance of 12 Å and the long-range Coulomb

potential beyond 12 Å is approximated by the Ewald[35] or particle-particle particle-mesh (PPPM) long-range solver[36] with the precision of 1e-5.

We then get 12 replicas of such cellulose (12 molecules, each with polymerization of 8, 2052 atoms in total) and align them randomly in an orthogonal box (as in Fig.2(a)) with the dimension of 100.87 Å × 102.24 Å × 83.37 Å. Based on the forcefield, this box is relaxed through molecular dynamics calculation in LAMMPS[37,38] for 400 ps under the periodic boundary conditions (in all 3 dimensions) and isothermal-isobaric (NPT) ensemble at 800 K and 0 Pa. The temperature of 800 K, which is right above the reported glass transition temperature of dry cellulose (500-650 K)[39], is adopted here to induce enough randomness in the alignment of the polymers and to form an amorphous phase. LAMMPS performs NPT time integration in default using Nose-Hoover style non-Hamiltonian equations of motion. The time step is 1 fs, while the time scale on which temperature and pressure are relaxed is set respectively as 100.0 fs and 500.0 fs. Three adjustable dimensions (x, y, z) in the simulation box are not coupled here to allow anisotropic deformation. Consequently, the box shrinks into a periodical cube full of amorphous cellulose with the dimension of 26.39 Å × 28.22 Å × 30.25 Å and the density of around 1160 kg/m^3. This state, which is denoted as PAC@800K (PAC stands for periodical AC matrix), is our starting point to construct the demanded hierarchical porous structure.

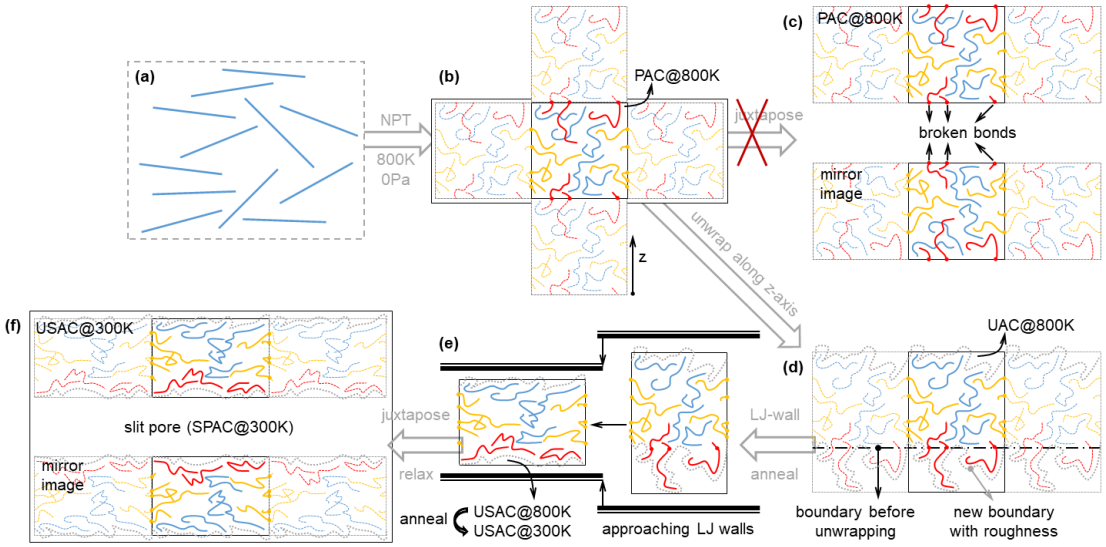

Fig 2 Workflow of the construction process of the slit-pore structure. The schematic is in 2D to facilitate intuitive understanding, while the real computational system is in 3D. Meanwhile, different colors are employed here to differentiate celluloses at different positions. That is, though in different colors, cellulose chains in this system are with the same physical and chemical properties. (a) Twelve Iβ crystallite celluloses with polymerization of 8 aligned randomly in the initial simulation box. (b) Amorphous cellulose with periodic boundary conditions obtained through high temperature relaxation, denoted as PAC@800K, which stands for periodical AC matrix. (c) Physically unreasonable slit-pores constructed directly via juxtaposing PAC@800K (d) Amorphous cellulose with rough z-surface obtained through unwrapping the PAC@800K along the z-direction, denoted as UAC@800K, which stands for unwrapped AC matrix. (e) Amorphous cellulose with smooth z-surface modified from UAC@800K via approaching LJ walls and the subsequent annealing, denoted as USAC@300K, which stands for unwrapped, smoothed AC matrix. (f) Slit-pore structure – SPAC@300K obtained through juxtaposing the USAC with its mirror image and sufficient relaxing.

As shown in Fig.2(b), PAC@800K is built under periodic boundary conditions with its bonds straddling the box boundaries. In this case, juxtaposing two same boxes of PAC@800K leads to physically unreasonable slit-pores (see Fig.2(c)). Therefore, before proceeding, PAC@800K has to be unwrapped along its z-axis, resulting in a structure, UAC@800K (UAC stands for unwrapped AC matrix), only periodical in the x and y directions. This operation inevitably decreases the material density and induces roughness on the z-surface (Fig.2(d)). To compensate, the unwrapped structure is then modified by two approaching 9-3 Lennard-Jones (LJ) walls (Fig.2(e)). Energy and kinetic parameters of the LJ-walls are carefully tuned in order to render the unwrapped AC with a smooth surface and the similar density as PAC once annealed to the temperature of interest (300 K in this work). The density of PAC@300K is around 1372 kg/m^3 as discussed in detail later. Here, based on the parameters listed in **Supplementary Information Note II**, the UAC@800K is modified to USAC@300K (USAC stands for unwrapped, smoothed AC matrix), with its roughness smoothed from 4.74 Å to 1.36 Å and (envelop) density condensed from 745 kg/m^3 to 1322 kg/m^3. Notably, for slab material like USAC, there is no natural definition of roughness or density. In the section of **Analysis Method**, the relevant definitions will be further clarified.

The USAC@300K is then juxtaposed with its mirror image as in Fig.2(f), and a mesoscopic slit-pore emerges between the two slabs. Finally, to create an artificial constraint on the pore dimension, which mimics the effect of the outer framework of the non-isolated slit-pore as in Fig.1, a spring connected across the center of mass (COM) of the two slabs is introduced. In this work, four different initial spring lengths (2.6 nm, 2.8 nm, 3.0 nm and 5.0 nm) are employed to assess the effect of the size of the slit-pore on sorption properties. Meanwhile, the spring constant is fixed at 139 N/m (200 kcal/mol×Å^2). The justification of this value is available in **Supplementary Information Note III**. After relaxation under 300 K and 0 Pa in LAMMPS for 100 ps, stable systems with hierarchical pore structures are obtained, denoted as SPAC@300K (SPAC stands for slit-pore buried in AC matrix)). The roughness and (envelop) density of the slab walls in SPAC@300K are equilibrated at 1.45 Å and 1159 kg/m^3 for all spring lengths, while the equilibrium distance between the COMs of the slabs is almost equal to the initial spring length regardless of the existence of inter-slab forces.

Apart from the slit-pore systems, the properties of bulk AC should also be calculated as benchmark. Such a benchmark system is easily obtained via annealing PAC@800K from 800 K to 300 K until its dimension further shrinks to 26.40 Å × 29.60 Å × 24.44 Å and its density stabilizes at around 1372 kg/m^3. This density, quite similar to those former reported (1400 kg/m^3)[25] for bulk AC, verifies the rationality of the employed forcefield. Furthermore, this density is close to the (envelop) density of the slab walls in the structure of USAC@300K, thanks to the appropriate parameters employed in LAMMPS in the construction of the approaching LJ-walls in Fig.2(e).

2.3 Calculation Method

In this study, we mainly focus on SPAC@300K. As shown in Fig.1(c), the SPAC, isolated along the z-direction, is located in the center of the simulation box. Apart from the demanded slit-pore, there are also gaps present between the slit-pore outer surfaces and the z-dimension box boundaries, which are artefacts due to the omission of surrounding bulk material. During the numerical adsorption process, water molecules accumulate also in these gaps. This part of adsorption must be assessed by post-processing and then subtracted from the overall adsorption.

Computational studies on the sorption property of AC should mimic as much as possible the

experimental conditions in sorption/strain isotherm measurement where the material is exposed to an isothermal-isobaric environment with controlled relative humidity (RH). Therefore, in this study, we employ a water reservoir with controlled RH, a 300 K-thermostat and a 0 Pa-barostat at the boundaries of the benchmark system PAC and the slit-pore systems SPAC with different pore sizes. Since the RH under specific temperature is solely correlated with water chemical potential by Eq.(2), such systems can be regarded as μPT-ensemble, where μ denotes the water chemical potential.

$$\mu = \mu_0 + RT\ln(RH), \mu_0 = -48.8 \text{ kJ mol}^{-1} \quad (2)$$

In this section, we first summarize the employed forcefield and then clarify the workflow, platform and parameters to implement the molecular simulation under μPT-ensemble (the so-called osmotic ensemble).

As mentioned before, OPLS-AA forcefield with 1.14*CM1A-LBCC partial atomic charges is employed to incorporate the forces acting in cellulose. Water molecules are described by SPC/E forcefield[40]. We note that the compatibility of the two forcefields (OPLS-AA&SPC/E) has been discussed extensively in the literatures[41,42]. The Lennard-Jones potential is cut off once beyond the distance of 12 Å and the long-range Columbian potential beyond 12 Å is approximated by the Ewald[35] or PPPM long-range solver[36] with the precision of 1e-5. The corresponding parameters, taken from former studies[34,40], are enumerated in **Supplementary Information Note I**. Mixed coefficients are derived implicitly by geometrical mixing rule.

The two most commonly-used molecular simulation methods, Molecular Dynamics (MD) and Monta Carlo (MC), provide no direct tools for μPT-ensemble calculation. However, based on literature[25], such systems can be studied by a hybrid GCMC-MD algorithm as in Fig.3. In more detail, GCMC (grand canonical MC) monitors water molecular variation with the water reservoir and 300 K-thermostat under constant volume (μVT-ensemble), while MD computes the deformation in systems with the 300K-thermostat and 0 Pa-barostat under constant water molecules (NPT-ensemble). Notably, for SPAC, there is no necessity to employ barostat at the z-boundaries due to the existing gaps between the solid matrixes and box boundaries. To ease the calculation burden, the dimension along the z-axis is kept constant. The GCMC and MD are then looped iteratively until the sorption and deformation reach their equilibrium, providing the solution for μPT-ensemble.

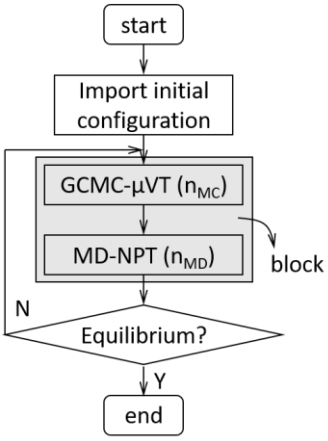

Fig 3 Hybrid GCMC-MD algorithm. To implement μPT-ensemble calculation, n_{MC} consecutive steps of GCMC and n_{MD} consecutive steps of MD are looped iteratively until the sorption and deformation reach their equilibrium.

To implement the process, Cassandra[43] (for GCMC) and LAMMPS[37,38] (for MD) are connected iteratively in virtue of the open-source package Pysimm[44]. LAMMPS performs NPT time integration using Nose-Hoover style non-Hamiltonian equations of motion. The time step is 1 fs, while the time scale on which temperature and pressure are relaxed is set respectively to 100.0 fs and 500.0 fs. Three adjustable dimensions (x, y, z) in the simulation box are not coupled here to allow anisotropic deformation. The long-range solver PPPM is faster than Ewald[36], but it is not available in CASSANDRA. Therefore, Ewald is employed in CASSANDRA, while PPPM in LAMMPS.

As shown in Fig.3, each iteration loop including several consecutive steps of GCMC and several consecutive steps of MD is called one block, with the specific GCMC steps n_{MC} and MD steps n_{MD} denoted as the block size. The normally adopted block size in this study is n_{MC} = 50000 and n_{MD} = 5000, except when the system is far from equilibrium. System performance during the adsorption phase is observed when the previously evacuated or equilibrated system is subjected to a water atmosphere with higher chemical potential. Particularly, when the system is totally dried up and suddenly subjected to a water reservoir, we will first gradually saturate it by operating several small blocks *with* n_{MC} = 5000 and n_{MD} = 2000 to avoid initial shock, and then resort to normal blocks. Detailed process data in **Fig.(S1-S12) in Supplementary Information** reveal that the systems undergo at least 3000-6000 normal blocks before reaching equilibrium.

2.4 Analysis Method

The coupled sorption-deformation properties of the uniform system of PAC can be unambiguously defined by the overall or specific sorption amount and volumetric strain[25]. However, in hierarchical pore structure like SPAC@300K, non-uniform sorption and desorption happen. In order to differentiate the sorption/deformation in different geometries and thus related to different mechanisms, it is imperative here to define the boundary of the pores and other critical geometric metrics.

As illustrated in Fig.4, each slab of wall is divided into $n_x \times n_y$ pieces of cuboid by evenly splitting the occupied domain into n_x and n_y sections along the x and y directions, respectively. The minimum and maximum z-coordinates occupied by the cellulose atoms belonging to the specific xy-section are then recorded as the down and up boundaries corresponding to this piece of cuboid. Consequently, the slab walls can be regarded as being delineated by these cuboids. The proximity between the cuboid-based boundaries and the practical slab boundaries are largely dictated by the employed section numbers n_x and n_y. Generally, larger section numbers correspond to a finer depiction of the boundaries. For this study focusing on water adsorption, a grid size comparable to the van de Waals radius of water molecules (2.5-4 Å) is employed, since micro-structure smaller than this value is almost non-accessible to moisture. Accordingly, n_x and n_y are set to be 10 so that the section length of the cuboid is around 3.5 Å.

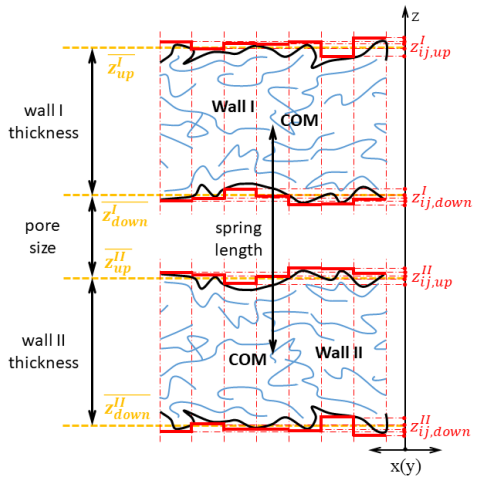

Fig 4 2D schematic of boundary definition in slit-pore structure. The occupied domain is evenly splitted into n_x and n_y sections along the x and y directions, respectively. The minimum and maximum z-coordinates occupied by the cellulose atoms belonging to the specific xy-section are then recorded as the down and up boundaries corresponding to this section. These down and up boundaries are considered as the discretized approximation to the pore boundaries of the slit-pore structure.

Based on this assumption, the wall thickness t, wall roughness r, pore size d, slit-pore surface area A, and slab volume v can be calculated using the following definitions:

$$t^W = \overline{z_{up}^W - z_{down}^W} = \frac{\sum_{i,j}\left(z_{ij,up}^W - z_{ij,down}^W\right)}{n_x n_y}, W \in \{I, II\} \tag{3}$$

$$r_B^W = \sqrt{\frac{\sum_{i,j}\left(z_{ij,B}^W - \overline{z_B^W}\right)^2}{n_x n_y}}, \overline{z_B^W} = \frac{\sum_{i,j} z_{ij,B}^W}{n_x n_y}, W \in \{I, II\}, B \in \{up, down\} \tag{4}$$

$$d = \overline{z_{down}^I - z_{up}^{II}} = \frac{\sum_{i,j}\left(z_{ij,down}^I - z_{ij,up}^{II}\right)}{n_x n_y} \tag{5}$$

$$A_B^W = l_x l_y + \sum_i \sum_j \left[\frac{l_x}{n_x}\left(z_{i(j+1),B}^W - z_{ij,B}^W\right) + \frac{l_y}{n_y}\left(z_{(i+1)j,B}^W - z_{ij,B}^W\right)\right], W \in \{I, II\}, B \in \{up, down\} \tag{6}$$

$$v_{eq}^W = l_x l_y t^W, W \in \{I, II\} \tag{7}$$

$$v_{ev}^W = l_x l_y \left[\max\left(z_{ij,up}^W\right) - \min\left(z_{ij,down}^W\right)\right], W \in \{I, II\} \tag{8}$$

where l_x and l_y denote the box length along the x and y direction, superscript W denotes the wall name (since there are two walls), and the subscript 'up' or 'down' is used to refer to up- or down-boundary of the specific wall.

There are two definitions for slab volume, one is the equilibrate volume equal to the overall volume of the constituting cuboids, which is dependent on the choice of n_x and n_y, while the other one is the envelop volume equal to the cuboid volume when $n_x = n_y = 1$. Definition of the cellulose density in

the slab walls can be naturally deduced by dividing the cellulose mass by slab volume. Respective to the two definitions of volume, we get equilibrate density and envelop density as well. Apart from these values, the distance along the z-direction between the COM of the two wall slabs, i.e., the spring length, is also an important parameter. All the above values are transient ones so that they must be constantly calculated and recorded throughout the process of calculation.

Water molecules can then be classified into water inside the wall matrices, inside the slit-pore and outside the structure (which is artefact as discussed before) based on the above definition. Specifically, the z-coordinate of the oxygen atom of a water molecule is compared with the delineating cuboids locally corresponding to the wall I and wall II. If the z-coordinate is above or below both the cuboids, the water is considered up or down outside the structure. On the contrary, if the z-coordinate lies in the gap between the two cuboids, the water is considered in the slit-pore. If neither outside the structure nor inside the pore, the water is considered as located inside the walls. However, other than absolute values, specific sorption amount and relative geometric change ratio respective to the initial SPAC structure are of more significance. Particularly, specific sorption amount in this system is denoted as water content, which is defined as the ratio between the adsorbed water mass within particular region and the overall cellulose mass. Regardless of the kind of water content considered (in the pores, inside the walls, outside or overall), the denominator used to calculate the water content is always the overall cellulose mass. Meanwhile, the relative geometric change ratio is denoted as length or volumetric strain, with its definition given in Eq.(9).

$$\varepsilon = \frac{G - G_0}{G_0} \tag{9}$$

where G represents the transient geometric value and G_0 refers to the corresponding initial value under zero water loading. The suitable geometric values in Eq.(9) include but are not limited to wall thickness, equilibrate volume and envelop volume.

To reduce statistical uncertainty, all the parameters of interest are derived by inserting sufficient sample points after convergence and averaging all these sample values. In this work, 500 extra blocks are conducted after the convergence and for each block 5 time-uniformly distributed sample points are examined. Errors of the calculated parameters are defined as the standard error of all these 2500 (5 × 500) sample points.

3 Results

3.1 Adsorption Isotherm

Fig.5(a) presents the water content versus RH inside the wall matrices and in the slit-pore, i.e., the overall water adsorbed amount in the structure per solid mass excluding the ones adhering to the outer walls. As we can see, all the four adsorption isotherms coincide with each other in the beginning, while the curves for the smaller slit-pores are subjected to a sudden increase in water content at a specific relative humidity. Notably, the smaller the slit-pore, the earlier this stepwise and the smaller offset can be observed. To be specific, the adsorption isotherm for the slit-pore with the original spring length of 2.6 nm jumps to a higher level at around 50% RH, whereas 2.8 nm at 70% RH and 3.0 nm at 90% RH. This jump in water content suggests the occurrence of capillary condensation. Based on the Laplace and Kelvin's law (Eq.(10)), the Laplace pressure or RH at which capillary condensation occurs for different slit-pore size can be determined.

$$\Delta p = \frac{2\gamma\cos\theta}{r_p} = \frac{RT}{V_m}\ln(RH) \tag{10}$$

where T, p, R, V_m, γ, θ and r_p denote temperature, hydrostatic pressure, ideal gas constant, water molar volume, water surface tension, water contact angle against air on AC and slit-pore size, respectively.

The reported water contact angle for cellulose (II) is around π/5 rad, however, amorphous cellulose with less ordered structure and rough surface may possess a larger value[45]. With water surface tension of 0.0728 N/m and water contact angle of π/3 rad, the RH at which capillary condensation occurs is around 50-60%, 60-70% and 70-80% for the slit-pores with the initial spring length of 2.6 nm, 2.8 nm and 3.0 nm. The predicted values are close to the range of the computational obtained values, showing agreement between theory and MD/GCMC calculation.

For the larger slit-pore with the original spring length of 5.0 nm, capillary condensation is found to happen near-saturation (RH ~ 1) or even super saturation (RH > 1). Before the jump in water content, all adsorption isotherms increase monotonously with RH. Compared with the benchmark adsorption isotherm of bulk AC, the slope of the curves before the stepwise increase is slightly smaller for lower humidity but slightly larger for higher humidity. After the stepwise increase, the adsorption isotherms undergo moderate increase.

Adsorption isotherms of the water adhering to the outer walls is shown in Fig.5(b). Within the margin of error, all the adsorption isotherms converge to a monotonously increasing concave curve. Such convergence is attributed to the same sorption mechanism of outer walls in the SPAC regardless of the difference in pore sizes, namely, surface covering.

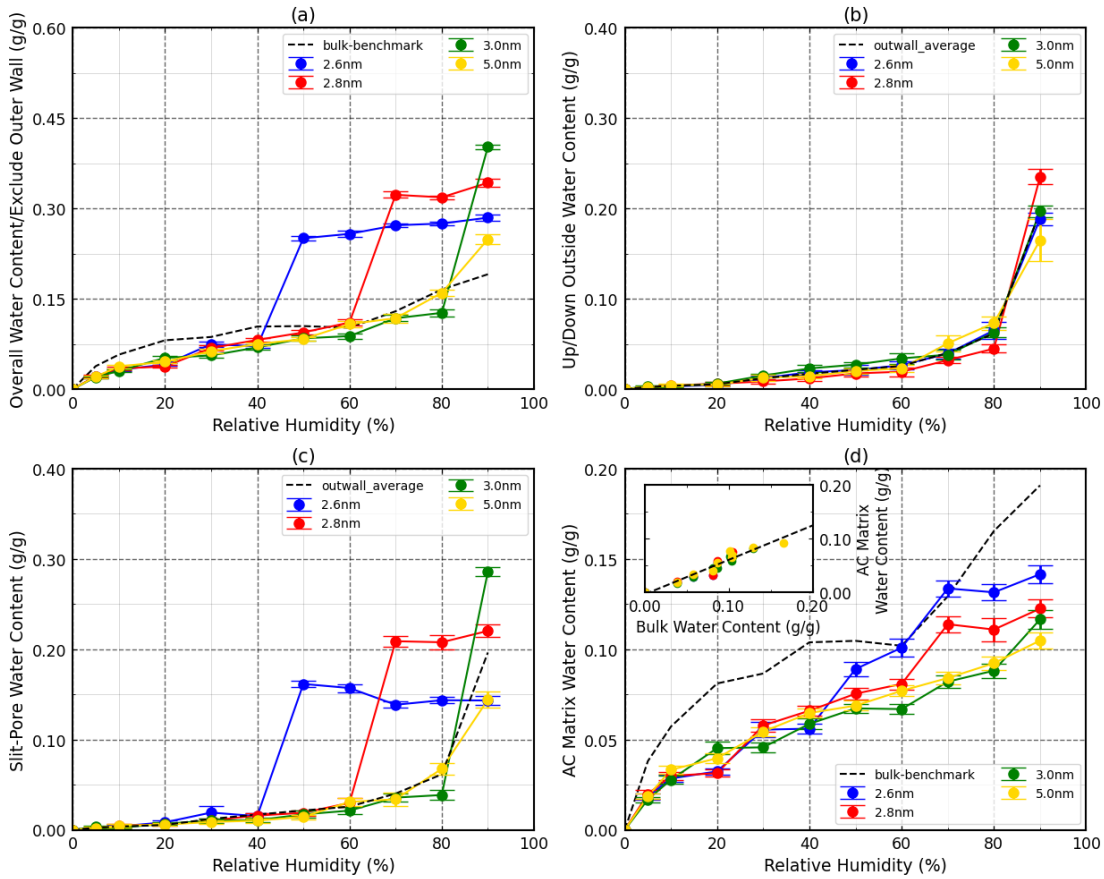

Fig 5 Adsorption isotherms for water molecules in different locations (in wall matrices, in slit-pores or on outer wall) of the slit-pore systems (a) Overall water content in AC matrix and in slit-pores excluding water on the outer wall (b) Water content on the outer walls of the SPAC (c) Slit-pore water content (d) AC matrix water content

Adsorbed water molecules in Fig.5(a) can be further decomposed into the water in the slit-pore and water in AC matrix, as shown in Fig.5(c) and Fig.5(d), respectively. These two figures share the same intriguing feature as in Fig.5(a), that is, all the curves corresponding to the different slit-pore sizes overlap at low RH but differ to different branches beyond a specific relative humidity. As mentioned before, the adsorption isotherm for the slit-pores with the original spring length of 2.6 nm, 2.8 nm, and 3.0 nm diverge at 50%, 70% and 90% RH, respectively. Although the divergence in Fig.5(c) is not surprising, the divergence in Fig.5(d) for the water content of the matrix is somewhat counter-intuitive, revealing a coupling between the capillary condensation in pores and the sorption in the slab walls and only understandable once the sorption-induced deformation is analyzed (see below).

The water adsorbed in slit-pores before capillary condensation conforms to a benchmark line in Fig.5(c), which is obtained by the averaging of the curves in Fig.5(b). Such conformity verifies the assumption that, before the stepwise increase, the adsorption in the slit-pore is due to surface covering. However, with the thickening of the adsorbed water layer, capillary condensation takes place between the AC matrices when the water molecules from the opposite covering merge to form a capillary bridge and then quickly occupy all the spaces inside the slit-pores. The water content is therefore mainly determined by the volume of the slit-pores, which is almost constant for the specific slit-pore size (dictated by spring length) but increases with the increasing slit-pore size (spring length).

In Fig.5(d), we also compare the water content in the matrices of SPAC with that in bulk AC. Curves before the capillary condensation are similar to the benchmark curve for bulk AC but with smaller values. This similarity in shape is further magnified by the subplot in Fig.5(d) where the water contents corresponding to the two different matrices of the SPAC and PAC are depicted against each other. The near-linear correlation in the subplot indicates the same mechanism of adsorption inside the two different matrices. On the other hand, the value difference can be attributed to the different exposure of matrix along the boundaries of the slab, which introduces different sorption induced deformations. The matrix sorption curves after capillary condensation deviate from each other, showing a higher moisture content for the smaller slit pore. This deviation is explained by the coupling between sorption and deformation, enhancing additional water adsorption in the matrix, as also discussed in detail below.

To sum up, adsorption in the AC matrix, surface covering and capillary condensation in the slit-pore coexist in the SPAC. Adsorption in the AC matrices prevails throughout all hygroscopic region, while the surface covering is negligible at lower RH and increases quickly with increasing RH. The resulting isotherm of SPAC beyond the capillary condensation range in Fig.5(a) is therefore slightly flattened at lower RH but sharpened at higher RH compared to bulk AC. Capillary condensation happens at different RH for different pore sizes as expected.

3.2 Sorption induced deformation

Fig.6(a) presents the change of the equilibrium spring length referred to as spring offset versus RH,

which is the difference in the averaged distance between the vibrating COMs of the two slabs at a specific RH from its initial value at zero RH. However, the standard errors of the COM-distance sample values are without explicit physical meaning (especially, they are not equal with the computational uncertainties of the equilibrium spring length as expected) and thus not depicted. In more detail, even for perfectly equilibrated systems, the spring length might drastically fluctuate around its equilibrium position. Such fluctuations are attributed to initial velocity rather than the equilibrium length variation.

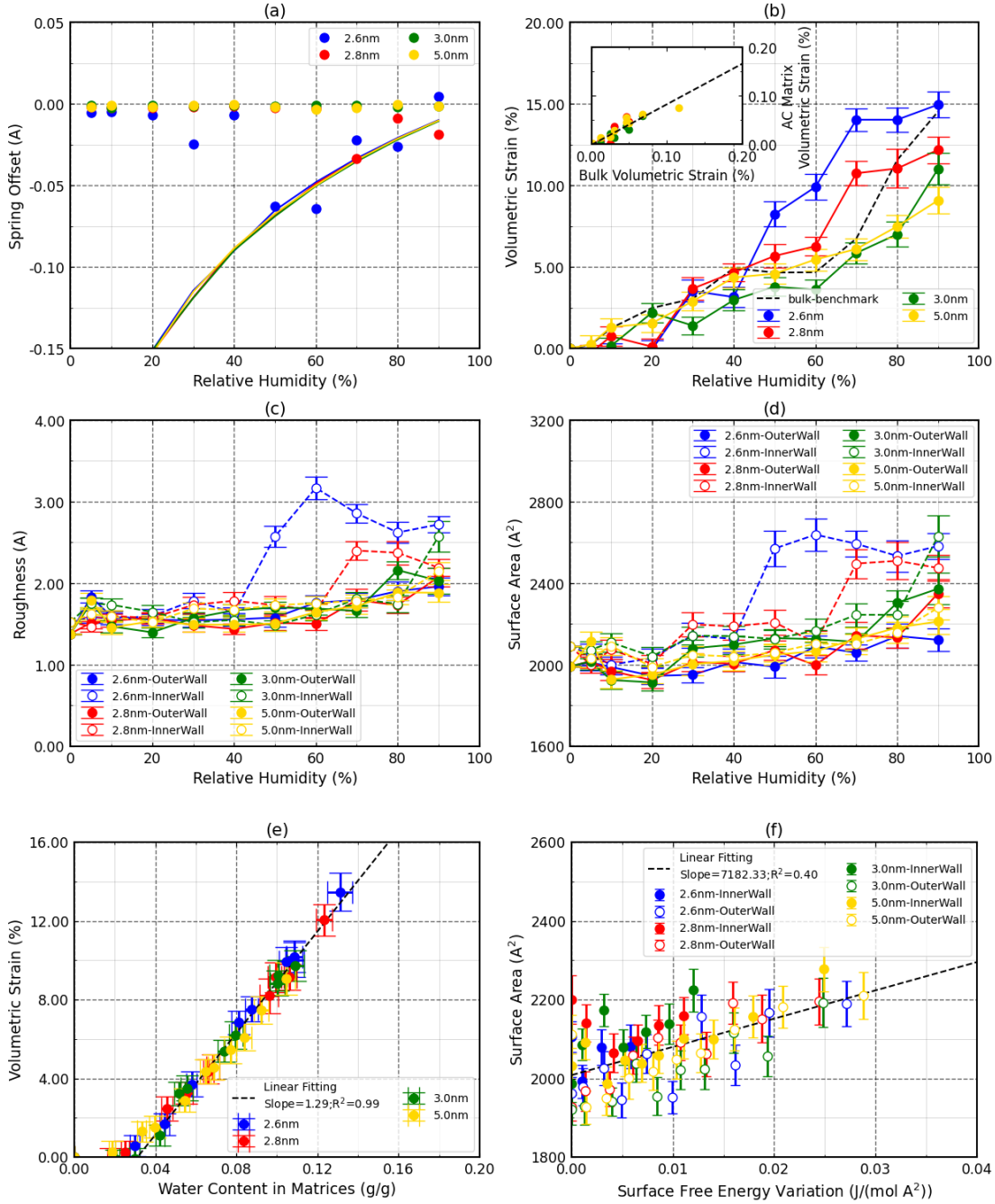

Fig 6 Sorption-induced deformation of the SPAC. (a) Variation of equilibrium spring length (b) Variation of volumetric strain of AC matrix (c) Variation of wall surface roughness (d) Variation of wall surface area (e) Correlation between the volumetric strain and water content of the AC matrix (f) Correlation between the surface area and the surface free energy variation of the slab surface

Based on Kelvin equation (Eq. (11)), when capillary condensation happens, the porous space will be saturated with water at negative hydrostatic pressure

$$\Delta p = \frac{RT}{V_m} \ln(RH) \tag{11}$$

where T, p, R, V_m denote temperature, hydrostatic pressure, ideal gas constant and water molar volume, respectively. This negative hydrostatic pressure induces a tensile force on the AC slabs towards the slit-pore. As a consequence, the spring connecting the COM of the two slabs will shrink to compensate for the pressure and to keep the system at force balance. The spring offset driven by capillary forces is determined as

$$\Delta l_s = \frac{l_x l_y}{k_s} \Delta p = \frac{RT}{V_m} \frac{l_x l_y}{k_s} \ln(RH) \tag{12}$$

where l_s and k_s denote equilibrated spring length and spring constant, respectively. In Fig.6(a), the spring offset during capillary condensation are well approximated by the solid lines as determined by Eq. (12), showing that the variation in spring length is attributed to capillary forces.

The volumetric strain of the AC matrix is demonstrated in Fig.6(b) to assess the slab deformation caused by adsorption in matrix and capillary condensation in slit-pore. Particularly, before capillary condensation, all matrices with different slit-pore sizes exhibit similar swelling with increasing RH.[24] We further depict the volumetric strain of the AC matrices in SPAC before the capillary condensation against the bulk volumetric strain of the benchmark PAC in the subplot of Fig.6(b). The near-linear relationship infers the similar deformation mechanism at play in AC matrix in SPAC and bulk AC, referred to as sorption-induced stress in literature[25]. However, once capillary condensation has occurred, matrix is subjected to a negative hydrostatic or tensile force and therefore an extra increase in volumetric strain. Moreover, in Fig.5(d), a simultaneous increase of matrix water content is observed, indicating a coupling between the sorption and deformation in matrix. In particular, due to the tensile forces on the matrix caused by capillary condensation, the matric pore space opens up allow additional access to water molecules. This effect is generally known in wood science literature as mechano-sorptive effect.

To conduct quantitative analysis, the volumetric strain in Fig.6(b) is plotted against the inside water content of the AC matrices from Fig.5(d). As shown in Fig.6(e), all the points collapse into one curve, which is convex at first but then linear. The convex part can be interpreted as an initial filling of the pre-existing porosity, while the linear part as a subsequent filling of the extra voids induced by swelling of the AC matrix due to the combined effects of sorption stress and capillary forces. Such collapse of the data suggests that the sorption stress in micropores or capillary forces in mesopores have a similar effect on AC matrix, leading to a unique correlation between water content and volumetric strain.

In **Fig.(S13) in Supplementary Information,** we also present the strain variation along each of the three dimensions. Compared with volumetric strain, strain pattern of the AC matrix along the x, y and z-axis shows some higher variation, maybe due to the limited size of MD computational domain. However, a general trend of swelling along the z-axis and shrinking along the xy-plane is observed, either with or without capillary condensation.

Such shrinkage seems to contradict Bangham's law, which suggests that surfaces subjected to water covering tends to increase its surface area. More specifically, the surface area enlargement is

assumed proportional to the surface energy variation, while the surface energy variation can be predicted by Gibbs' adsorption isotherm (Eq.(1)). The following section tries to demonstrate that the in-plane shrinkage and surface area enlargement may coexist in our systems.

In systems composed of flexible polymers like SPAC, shrinkage in in-plane direction may be accompanied by an increase in surface area due to an increase in local roughness or irregularity. Such behavior may be visualized as accordion effect in Fig.7. Fig.7(c) and Fig.7(d) show snapshots of the dry surface of the matrix and of the surface subjected to moisture load with their contour lines projected on the xy-plane. It is clearly observed that, while shrinkage occurs in the in-plane directions, the surface area increases due to the augmented local roughness or irregularity. A sketch of the accordion effect is given, showing the initial dry rough surface (Fig.7(a)) which shrinks in in plane-direction and swells in normal direction upon adsorption of water molecules (Fig.7(b)). Fig.6(c) and Fig.6(d) depict the variation of wall surface roughness and surface area with RH. As shown, the roughness and surface area of the outer walls increase monotonously with the progress of water covering. The same trend is observed for the inner slit-pore surfaces before the capillary condensation.

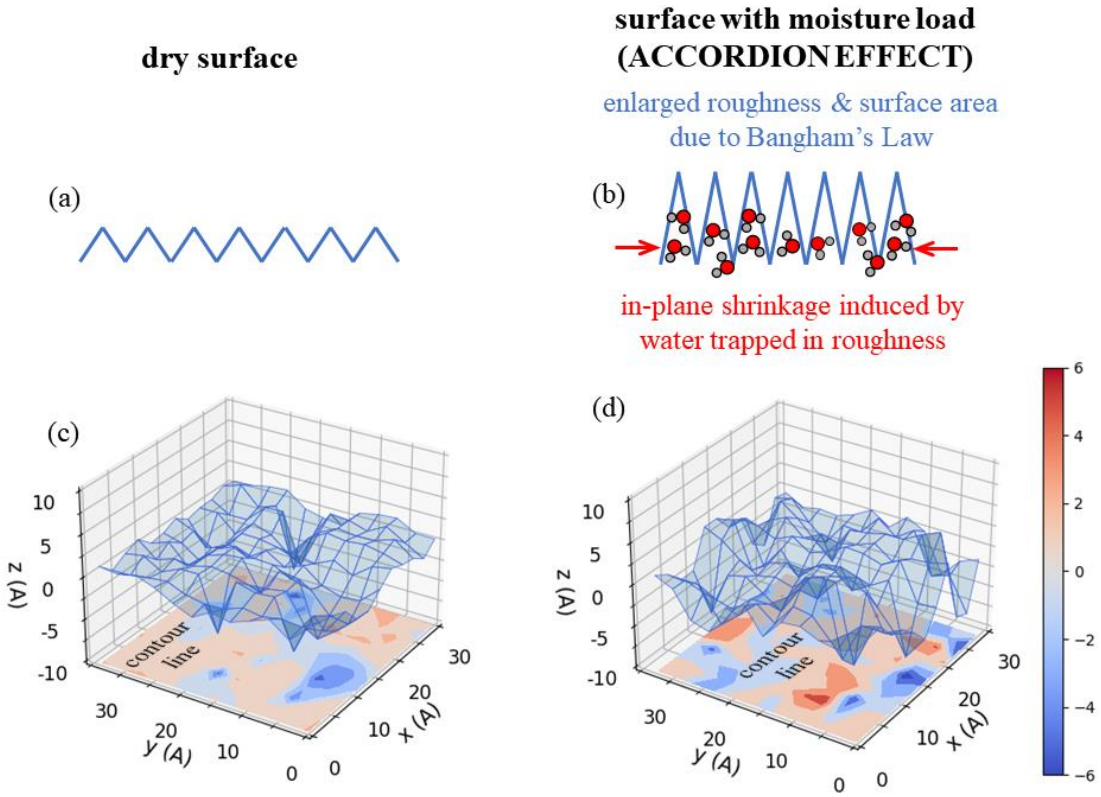

Fig.7 Schematic of Accordion Effect. (a) schematic dry surface (b) schematic surface with moisture load, enlarged roughness and in-plane shrinkage (c) snapshot of the dry surface with its contour line projected on the xy-plane (d) snapshot of the surface with moisture load with its contour line projected on the xy-plane

Fig.6(f) displays the relationship between the surface area and the surface free energy variation in SPAC. To be specific, free energy variation of the surface, initially defined as an integral formula by Gibbs' adsorption isotherm (Eq.(1)), is approximated here by an equation of summation (Eq.(13)).

$$\Delta\gamma\left(RH_J\right)=-\int_{-\infty}^{\mu}\frac{N\left(\mu^*\right)}{A\left(\mu^*\right)}d\mu^*=\sum_{i=1}^{J}\frac{N\left(RH_i\right)}{A\left(RH_i\right)}RT\left[\ln\left(RH_i\right)-\ln\left(RH_{i-1}\right)\right] \quad (13)$$

where γ, N and A denote water surface tension, the number of water molecules in the surface covering layer and the surface area, respectively. The surface energy variation (absolute value) at the specific RH_J derived by Eq.(13) is then depicted with the corresponding surface area in Fig.6(f). Though with non-negligible deviation, points in Fig.6(f) seemingly conform to a linear pattern, validating the applicability of Bangham's law in the SPAC system showing in-plane shrinkage.

The shrinkage along in-plane direction as observed in this study can be explained by the appearance of attractive solid–fluid forces when a rough surface becomes covered with water molecules, as described in literature[46]. Along the x- and y-direction, this surface stress triumphs the swelling stress induced by the sorption in matrix, leading to an overall in-plain shrinkage. On the other hand, the swelling of the matrix in z-direction before capillary condensation is dominated by the swelling of the bulk AC and not counteracted by the surface effects. This phenomenon, referred to as accordion shrinkage effect, is an intriguing topic which needs more in depth analysis beyond the discussion in this work.

4. Discussion

This work reveals the coupling mechanism between the sorption and deformation in a prototype hierarchical porous structure featured with a mesoscopic slit-pore surrounded by hydrophilic, amorphous and microporous polymers. Based on former studies, some basic characteristics of the sorption and sorption-induced deformation in natural or artificial desiccant with hierarchical porous structure are inferable. First, with increasing ambient humidity, the microporous material will be gradually saturated with water molecules, first in the pre-existing micropores and then in the sorption-induced extra microporous space. Meanwhile, surface covering with water molecules takes place on the exposed surface surrounding the mesopores, in this case the slit-pore, or even macropores. As a material composed of flexible biopolymers, increase in local roughness or irregularity may be induced in the polymeric and soft surface to respond to the surface free energy reduction by surface covering. Beyond a specific RH, the water layer on the surfaces of mesopores reconfigures and capillary condensation happens, imposing a negative capillary or tensile force on its encompassing materials. The length or volumetric strain of the polymeric matrix is thus attributed to the coupling of the sorption-induced stress in micropores and the negative capillary force in mesopores. The extra strain induced by the capillary force will lead to a supplementary increase in water content.

However, due to the difference between our prototype model and the real polymer desiccant with more sophisticated component or porous structure, the above data are not sufficient for the comprehensive understanding or quantitative prediction of sorption behavior of wood cell wall. In the following, the simplifications and limitations in this study are summarized, in order to pave the way for further research.

First of all, our study employs slabs with homogenous, pure substance, namely, several chains of amorphous cellulose with the polymerization of 8. However, the actual matrix of wood cell wall is a heterogeneous composite consisting of crystalline cellulose, different types of hemicellulose and lignin. Moreover, all polymers are in different sizes of polymerization, ranging from 100 to 10000. The abundance of chemical components in practical material will induce complicated phenomena

like heterogeneous sorption due to the difference in hydrophilicity among components, anisotropic deformation due to the difference in stiffness among components and possible coupling at the interfaces between different components.

Real cell wall material also features more complicated geometric structure. As in literature, natural fiber can be regarded as a network of multi-scale hierarchical connecting pores with different sizes and geometrics. In our study, however, only an isolated, nanoscale slit-pore is examined and the observation based on such simplification is subjected to at least three limitations. The first is the lacking of discussion on the influence of pore shape. The second is the size effect due to the limited size of the MD domain. Notably, this study focuses on a nano-scale slit-pore periodical along the xy-plane but isolated along the z-direction with thin walls. Forces from atoms in the outer domain of the slit-pore as shown in Fig.1(a) are omitted and simply substituted by a spring with constant original length and stiffness. Such substitution captures the long-range constrictions of the outer framework imposed on the slit-pore, but sacrifices the local atomic interaction along the cut-off interface and the possible mechanical weakening of the practical outer framework upon sorption. The third is the oversight on the coupling between different connecting pores.

Last but not least, the analysis methods in this study can be further improved. Notably, the boundaries of the slit-pores are approximated by the outlines of a set of discretized cuboids, resulting in the simple definitions of thickness, surface area and volume, which are dependent on the discretization size. Moreover, the definition of roughness above cannot fully capture the features of the surface profile of the slab walls, thus is limited in conveying detailed information. In future, we aim at studying in more detail the accordion shrinkage effect and its impact on sorption-induced deformation. Based on this understanding, we can further upscale the data towards a poromechanical model allowing to predict the sorption induced deformations at macroscale.

5. Conclusion

In this work, we built a hypothetical, hierarchical porous structure at the atomic level and then evaluated its compositional and structural evolution during water vapor sorption using molecular simulation. In microscopic pores prevailing in the amorphous cellulose matrix, water filling of micropores happens throughout the full RH range. Under low RH, adsorption happens mainly by filling existing voids. At high RH, adsorption continues via imposing a sorption stress, leading to a swelling and additional sorption of the microporous material. In the mesoscopic slit-pore between the two cellulose slabs, surface sorption takes place with negligible adsorbed amount initially but remarkable thickness with increasing RH. Meanwhile, a simultaneous increase of the local roughness and the overall surface area of slabs is observed, in response to a decreased surface energy as surface covering occurs. The correlation between the surface area and the surface free energy variation is well captured by Bangham's law. However, opposed as often reported, surface covering of the rough surface of amorphous cellulose boundaries is accompanied with shrinkage explained as accordion effect. At a certain RH, the water molecules residing on the opposite cellulose slabs undergo capillary condensation, which exerts a negative hydrostatic pressure or tensile force on the AC matrices, resulting in an increase in matrix porosity and water content, a decrease in distance between the center of mass (COM) of the slabs and thus a thinning of the slit-pore. The induced porous space in slabs, either by sorption stress in matrices or capillary forces in slit-pores, is saturated with water once created.

Acknowledgement

We thank Shanghai Jiao Tong University for its financial support on this work and also project 'intoS2' NO.182512 funded by SNF together with ANR, PIs Derome Chabbert.

Reference

1. Chen, C. *et al.* Structure–property–function relationships of natural and engineered wood. *Nat Rev Mater* **5**, 642–666 (2020).
2. Zhu, H. *et al.* Wood-Derived Materials for Green Electronics, Biological Devices, and Energy Applications. *Chem Rev* **116**, 9305–9374 (2016).
3. Liu, S. *et al.* Bioinspired thermochromic transparent hydrogel wood with advanced optical regulation abilities and mechanical properties for windows. *Appl Energy* **297**, 117207 (2021).
4. Nyholm, L., Nyström, G., Mihranyan, A. & Strømme, M. Toward Flexible Polymer and Paper-Based Energy Storage Devices. *Advanced Materials* **23**, 3751–3769 (2011).
5. Ma, J., Li, X. & Bao, Y. Advances in cellulose-based superabsorbent hydrogels. *RSC Adv* **5**, 59745–59757 (2015).
6. Wang, W., Yang, S., Zhang, A. & Yang, Z. Preparation and properties of novel corn straw cellulose–based superabsorbent with water-retaining and slow-release functions. *J Appl Polym Sci* **137**, 48951 (2020).
7. Jiang, Y., Lawrence, M., Ansell, M. P. & Hussain, A. Cell wall microstructure, pore size distribution and absolute density of hemp shiv. *R Soc Open Sci* **5**, 171945 (2018).
8. Kojiro, K., Miki, T., Sugimoto, H., Nakajima, M. & Kanayama, K. Micropores and mesopores in the cell wall of dry wood. *Journal of Wood Science* **56**, 107–111 (2010).
9. Gao, X., Zhuang, S., Jin, J. & Cao, P. Bound water content and pore size distribution in swollen cell walls determined by NMR technology. *Bioresources* **10**, 8208–8224 (2015).
10. Pidgeon, L. M. & Maass, O. The adsorption of water by wood. *J Am Chem Soc* **52**, 1053–1069 (1930).
11. Shi, J. & Avramidis, S. Water sorption hysteresis in wood: I review and experimental patterns – geometric characteristics of scanning curves. **71**, 307–316 (2017).
12. Thygesen, L. G., Tang Engelund, E. & Hoffmeyer, P. Water sorption in wood and modified wood at high values of relative humidity. Part I: Results for untreated, acetylated, and furfurylated Norway spruce. **64**, 315–323 (2010).
13. Engelund, E. T., Thygesen, L. G. & Hoffmeyer, P. Water sorption in wood and modified wood at high values of relative humidity. Part 2: Appendix. Theoretical assessment of the amount of capillary water in wood microvoids. **64**, 325–330 (2010).
14. Thommes, M. *et al.* Physisorption of gases, with special reference to the evaluation of surface area and pore size distribution (IUPAC Technical Report). **87**, 1051–1069 (2015).
15. Harris, J. M. & Meylan, B. A. The Influence of Microfibril Angle on Longitudinal and Tangential Shrinkage in Pinus radiata. **19**, 144–153 (1965).
16. Badel, E., Bakour, R. & Perré, P. Investigation of the Relationships between Anatomical Pattern, Density and Local Swelling of Oak Wood. *IAWA J* **27**, 55–71 (2006).
17. Derome, D., Griffa, M., Koebel, M. & Carmeliet, J. Hysteretic swelling of wood at cellular scale probed by phase-contrast X-ray tomography. *J Struct Biol* **173**, 180–190 (2011).
18. Hernández, R. E. Influence of moisture sorption history on the swelling of sugar maple wood and some tropical hardwoods. *Wood Sci Technol* **27**, 337–345 (1993).

19. Chen, M., Coasne, B., Guyer, R., Derome, D. & Carmeliet, J. A Poromechanical Model for Sorption Hysteresis in Nanoporous Polymers. *J Phys Chem B* **124**, 8690–8703 (2020).
20. Ciesielski, P. N. *et al.* 3D Electron Tomography of Pretreated Biomass Informs Atomic Modeling of Cellulose Microfibrils. *ACS Nano* **7**, 8011–8019 (2013).
21. Charlier, L. & Mazeau, K. Molecular Modeling of the Structural and Dynamical Properties of Secondary Plant Cell Walls: Influence of Lignin Chemistry. *J Phys Chem B* **116**, 4163–4174 (2012).
22. Zhang, C. *et al.* Hygromechanical mechanisms of wood cell wall revealed by molecular modeling and mixture rule analysis. *Sci Adv* **7**, eabi8919 (2023).
23. Zhang, C. *et al.* Hygromechanics of softwood cellulosic nanocomposite with intermolecular interactions at fiber-matrix interface investigated with molecular dynamics. *Compos B Eng* **228**, 109449 (2022).
24. Zhang, C., Chen, M., Keten, S., Derome, D. & Carmeliet, J. Towards unraveling the moisture-induced shape memory effect of wood: the role of interface mechanics revealed by upscaling atomistic to composite modeling. *NPG Asia Mater* **13**, 74 (2021).
25. Chen, M., Coasne, B., Derome, D. & Carmeliet, J. Coupling of sorption and deformation in soft nanoporous polymers: Molecular simulation and poromechanics. *J Mech Phys Solids* **137**, 103830 (2020).
26. Kulasinski, K., Guyer, R., Keten, S., Derome, D. & Carmeliet, J. Impact of Moisture Adsorption on Structure and Physical Properties of Amorphous Biopolymers. *Macromolecules* **48**, 2793–2800 (2015).
27. Brochard, L., Vandamme, M., Pellenq, R. J.-M. & Fen-Chong, T. Adsorption-Induced Deformation of Microporous Materials: Coal Swelling Induced by CO2–CH4 Competitive Adsorption. *Langmuir* **28**, 2659–2670 (2012).
28. Kowalczyk, P., Ciach, A. & Neimark, A. v. Adsorption-Induced Deformation of Microporous Carbons: Pore Size Distribution Effect. *Langmuir* **24**, 6603–6608 (2008).
29. Chen, M., Coasne, B., Guyer, R., Derome, D. & Carmeliet, J. Molecular Simulation of Sorption-Induced Deformation in Atomistic Nanoporous Materials. *Langmuir* **35**, 7751–7758 (2019).
30. Coasne, B. & Ugliengo, P. Atomistic Model of Micelle-Templated Mesoporous Silicas: Structural, Morphological, and Adsorption Properties. *Langmuir* **28**, 11131–11141 (2012).
31. Vandamme, M., Brochard, L., Lecampion, B. & Coussy, O. Adsorption and strain: The CO2-induced swelling of coal. *J Mech Phys Solids* **58**, 1489–1505 (2010).
32. Gomes, T. C. F. & Skaf, M. S. Cellulose-Builder: A toolkit for building crystalline structures of cellulose. *J Comput Chem* **33**, 1338–1346 (2012).
33. Dodda, L. S., Vilseck, J. Z., Tirado-Rives, J. & Jorgensen, W. L. 1.14*CM1A-LBCC: Localized Bond-Charge Corrected CM1A Charges for Condensed-Phase Simulations. *J Phys Chem B* **121**, 3864–3870 (2017).
34. Dodda, L. S., Cabeza de Vaca, I., Tirado-Rives, J. & Jorgensen, W. L. LigParGen web server: an automatic OPLS-AA parameter generator for organic ligands. *Nucleic Acids Res* **45**, W331–W336 (2017).
35. Toukmaji, A. Y. & Board, J. A. Ewald summation techniques in perspective: a survey. *Comput Phys Commun* **95**, 73–92 (1996).
36. Isele-Holder, R. E., Mitchell, W. & Ismail, A. E. Development and application of a particle-

particle particle-mesh Ewald method for dispersion interactions. *J Chem Phys* **137**, 174107 (2012).

37. Plimpton, S. Fast Parallel Algorithms for Short-Range Molecular Dynamics. *J Comput Phys* **117**, 1–19 (1995).
38. Thompson, A. P. *et al.* LAMMPS - a flexible simulation tool for particle-based materials modeling at the atomic, meso, and continuum scales. *Comput Phys Commun* **271**, 108171 (2022).
39. Paes, S. S. *et al.* The glass transition and crystallization of ball milled cellulose. *Cellulose* **17**, 693–709 (2010).
40. Berendsen, H. J. C., Grigera, J. R. & Straatsma, T. P. The missing term in effective pair potentials. *J Phys Chem* **91**, 6269–6271 (1987).
41. Walter, J., Ermatchkov, V., Vrabec, J. & Hasse, H. Molecular dynamics and experimental study of conformation change of poly(N-isopropylacrylamide) hydrogels in water. *Fluid Phase Equilib* **296**, 164–172 (2010).
42. Hess, B. & van der Vegt, N. F. A. Hydration Thermodynamic Properties of Amino Acid Analogues: A Systematic Comparison of Biomolecular Force Fields and Water Models. *J Phys Chem B* **110**, 17616–17626 (2006).
43. Shah, J. K. *et al.* Cassandra: An open source Monte Carlo package for molecular simulation. *J Comput Chem* **38**, 1727–1739 (2017).
44. Fortunato, M. E. & Colina, C. M. pysimm: A python package for simulation of molecular systems. *SoftwareX* **6**, 7–12 (2017).
45. Dankovich, T. A. & Gray, D. G. Contact Angle Measurements on Smooth Nanocrystalline Cellulose (I) Thin Films. *J Adhes Sci Technol* **25**, 699–708 (2011).
46. Chen, M. & Ke, L.-L. Surface morphology regulates the sorption-induced deformation of mesoporous media. *Microporous and Mesoporous Materials* **335**, 111822 (2022).